

Interchain-Expanded Vanadium Tetrasulfide with Fast Kinetics for Rechargeable Magnesium Batteries

Cunyu Pei,[†] Yameng Yin,[†] Ruimin Sun,[†] Fangyu Xiong,[†] Xiaobin Liao,^{†,‡} Han Tang,[†] Shuangshuang Tan,[†] Yan Zhao,[‡] Qinyou An,^{*,†} and Liqiang Mai^{*,†}

[†]State Key Laboratory of Advanced Technology for Materials Synthesis and Processing and [‡]State Key Laboratory of Silicate Materials for Architectures, Wuhan University of Technology, Wuhan, Hubei 430070, China

Supporting Information

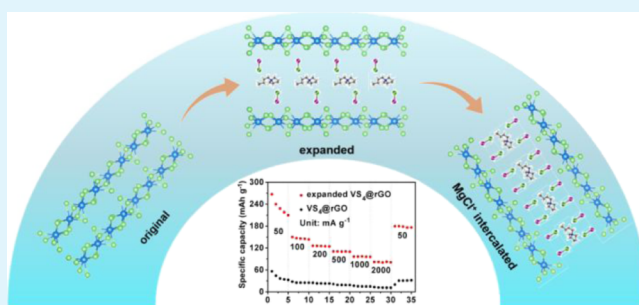
ABSTRACT: Magnesium batteries are promising energy storage systems because of the advantages of low raw material cost, high theoretical capacity, and high operational safety properties. However, the divalent Mg^{2+} has a sluggish kinetic in the cathode materials which resulted in poor electrochemical performance. Many strategies were adopted to improve the mobility of Mg^{2+} in the host structures. In this paper, we report on the optimization of chain-like structure VS_4 @reduced graphene oxide (VS_4 @rGO) through expanding interchain distance to increase the ion diffusivity. By combining theoretical calculations and experimental investigations, the expansion of interchain distance and reversible intercalation of MgCl^+ are revealed. With the fast kinetics of MgCl^+ (instead of Mg^{2+}) intercalation into expanded VS_4 @rGO, higher capacity of $268.3 \text{ mA h g}^{-1}$ at 50 mA g^{-1} and better rate capability of 85.9 mA h g^{-1} at 2000 mA g^{-1} have been obtained. In addition, the expanded VS_4 @rGO framework shows a high specific capacity of $147.2 \text{ mA h g}^{-1}$ after 100 cycles and a very wide operating temperature range (-35 to $55 \text{ }^\circ\text{C}$). The high discharge capacity, excellent rate capability, and broad temperature adaptability demonstrate promising application of VS_4 @rGO in magnesium batteries.

KEYWORDS: interchain-expanded, VS_4 @rGO, MgCl^+ , fast kinetics, magnesium battery

INTRODUCTION

Currently, Li-ion batteries (LIBs) have achieved great progress in the last few decades; however, the unsolved Li-dendritic problem and unsustainability and high cost of lithium source impede their rapid development in recent years.^{1–4} The rechargeable multivalent batteries (such as Mg-, Zn-, and Al-based batteries) have attracted increasing interest as promising energy storage sources because of the advantages of low cost, high energy density, and high safety properties. Therefore, they can be better options for large-scale energy storage systems.^{5,6} Among them, the Mg battery (MB) technology has gained tremendous research attention for the unique properties of Mg anodes, such as high volumetric capacity and large reserves in the earth.^{7–9} More remarkably, the Mg metal is resistant to the formation of dendritic structures owing to its unique electrodeposition behavior as well as high coulombic efficiency in suitable electrolytes.^{10–12} Other anode materials such as $\text{Li}_4\text{Ti}_5\text{O}_{12}$, Bi, and bismuth oxyfluoride as well as some specific optimization strategies were also reported, and excellent electrochemical performance was obtained.^{13–15}

However, in an effort to search for high-performance Mg-cathodes, the sluggish kinetics originated from the stronger polarizing nature between divalent Mg^{2+} and host materials is a big obstacle.^{16–18} In most cases, the conventional cathodes, which are mature in LIBs, exhibit low or even no capacities in



MBs.¹⁹ Up to now, the Chevrel phase (CP) Mo_6S_8 reported by Aurbach et al. had demonstrated excellent cycling stability (over 2000 cycles with little capacity loss) and reasonable kinetics of Mg^{2+} , which has been the benchmark for MBs, despite its uncompetitive low working voltage (ca. 1 V vs Mg/Mg^{2+}) and discharge capacity (ca. 100 mA h g^{-1}).^{20,21} Benefited from the unique structure, CP compounds have many vacant sites to accommodate Mg^{2+} , and the inserted divalent charge can be easily compensated by the valence change of Mo. As a result, the highly reversible Mg^{2+} insertion/extraction reactions can be realized.^{18,22} Nevertheless, the sluggish kinetics is still a challenging problem in other cathode materials, and many optimization strategies were adopted to improve the solid-state diffusion of Mg^{2+} in host materials.^{23–26} Recently, Yao and co-workers reported on the in situ expansion of TiS_2 and achieved high reversible capacity and excellent rate capability associated with MgCl^+ intercalation mechanism;²⁷ our group used a facile ultrasonicated exfoliation and self-assembly method to expand the layer spacing of VOPO_4 , leading to an outstanding electrochemical performance enabled by MgCl^+ intercalation.²⁸ Up to now, the

Received: June 2, 2019

Accepted: August 7, 2019

Published: August 7, 2019

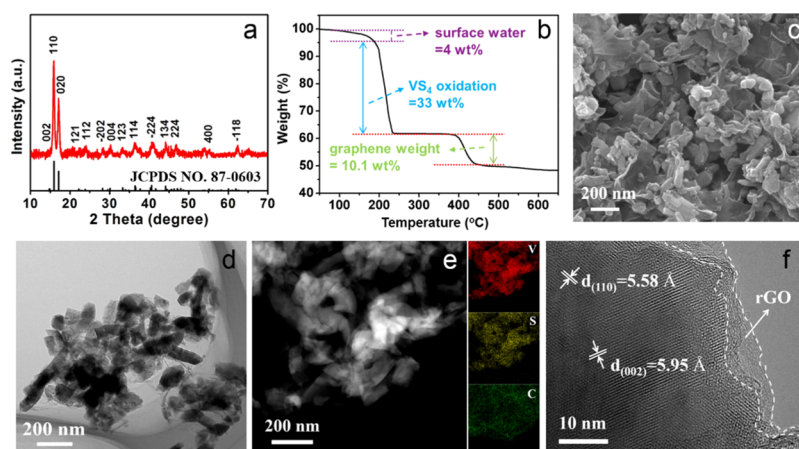


Figure 1. Structural and morphological characterization of $\text{VS}_4@\text{rGO}$. (a) XRD pattern, (b) TGA curve, (c) SEM image, (d) TEM image, (e) EDS-mapping, and (f) HRTEM image.

interlayer-expanded strategy was proposed to optimize the performance of layered materials. However, the modification on other crystal structure materials is rarely reported. It is well known that VS_4 is consisted of chainlike fragments connected by weak dispersive force, and the interchain distance is as high as 5.83 Å which is comparable to the interlayer distance (such as layered VS_2 , 5.8 Å). The neighboring chains can be pushed apart to a certain degree.²⁹ It is effective but challenging to obtain interchain-expanded VS_4 accompanied with enhanced performance when used as the cathode material for MBs.

Herein, we present the optimization strategy for VS_4 through pre-intercalation of $[\text{BMP}]^+$ (1-butyl-1-methylpyrrolidinium chloride, $[\text{BMP}]\text{Cl}$). With the intercalation of $[\text{BMP}]^+$, the interchain distances of VS_4 are expanded, thus higher capacity and enhanced rate performance have been obtained. Energy-dispersive spectroscopy (EDS) and X-ray photoelectron spectroscopy (XPS) analysis show the pre-intercalation of $[\text{BMP}]^+$ and reversible intercalation of MgCl^+ . The galvanostatic intermittent titration technique (GITT) tests demonstrate faster kinetics of MgCl^+ in $\text{VS}_4@\text{reduced graphene oxide}$ ($\text{VS}_4@\text{rGO}$) than that of Mg^{2+} , resulting in a great improvement of the reversible capacity and rate capability. Furthermore, in situ X-ray diffraction (XRD), ex situ Fourier transform infrared (FTIR), and Raman investigations were performed to characterize the structural evolution during the electrochemical MgCl^+ (de)intercalation in following cycles.

EXPERIMENTAL SECTION

Synthesis of $\text{VS}_4@\text{rGO}$. The $\text{VS}_4@\text{rGO}$ was synthesized through a similar hydrothermal reaction reported in previous publications.^{30,31} First, 0.366 g sodium metavanadate and 0.240 g sodium hydroxide were dissolved in the mixture of 22.5 mL GO (2.0 mg mL^{-1} , purchased from XFANO company) and 7.5 mL deionization (DI) water. At the same time, 1.127 g thioacetamide was dissolved in the mixture of 7.5 mL GO and 2.5 mL DI water. After continuous stirring, the two as-obtained solutions were mixed together and stirred for 1 h. Then, the final suspension was transferred to a 50 mL Teflon-lined autoclave and kept at 160 °C for 24 h. After cooling naturally, the products were collected and washed with DI water several times and finally dried in vacuum at 60 °C for 6 h.

Preparation of Electrolytes. The all-phenyl-complex (APC) electrolyte, a solution of 0.25 M $[\text{Mg}_2\text{Cl}_3]^+[\text{AlPh}_2\text{Cl}_2]^-$ /tetrahydrofuran (THF), was prepared according to Mizrahi et al.³² A suitable amount of $[\text{BMP}]\text{Cl}$ (purchased from Macklin) was added in the APC electrolyte to obtain the concentration of 0.25 M.

Material Characterization. XRD and in situ XRD measurements for the samples were performed using a D8 Advance X-ray diffractometer with a $\text{Cu K}\alpha$ X-ray source. Field-emission scanning electron microscopy (SEM) images were collected with a JEOL-7100F microscope. Transmission electron microscopy (TEM), high-resolution TEM (HRTEM), scanning TEM-high-angle annular dark-field (HAADF) images, and EDS were recorded by using a Titan G2-300 instrument. Thermogravimetric analysis (TGA) was performed using a NETZSCH-STA449F5 thermoanalyzer. Raman spectra were obtained using Renishaw inVia micro-Raman spectroscopy. FTIR spectra were recorded by using a Nicolet 60-SXB IR spectrometer. XPS measurements were obtained using a VG Multilab 2000 instrument. Inductively coupled plasma (ICP) measurements were conducted using a PerkinElmer Optima 4300DV spectrometer.

Measurement of Electrochemical Performance. The electrochemical properties were measured by assembling 2016 coin-type cells in a glovebox filled with pure argon gas, using a Mg foil as the anode, APC with and without $[\text{BMP}]\text{Cl}$ as electrolytes, and glass fiber as the separator. The three-electrode beaker cells were conducted in an argon atmosphere. All of the three electrodes were polished correctly and rinsed with distilled water and acetone before they were used. Cathode electrodes were fabricated with 70% $\text{VS}_4@\text{rGO}$ as the active material, 20% of acetylene black, and 10% of polytetrafluoroethylene. Galvanostatic discharge/charge cycling of the cells was performed in a potential range of 0.2–2 V versus Mg/Mg^{2+} with a multichannel battery testing system (LAND CT2001A).

RESULTS AND DISCUSSION

First, XRD was performed to identify the crystallinity of $\text{VS}_4@\text{rGO}$ composites. As shown in Figure 1a, all the peaks are consistent with the monoclinic VS_4 phase (JCPDS no. 87-0603). The mass change of $\text{VS}_4@\text{rGO}$ with the gradually increasing of temperature is exhibited in Figure 1b. The TGA curve exhibits three processes of mass loss. The first process (4 wt %) observed below 190 °C is caused by the removal of absorbed water; the second process (33 wt %) between 190 and 240 °C may result from the reaction of VS_4 and O_2 ;³³ and the third process (10.1 wt %) from 380 to 450 °C is caused by the burning of rGO. Figure 1c–e shows the morphology of the $\text{VS}_4@\text{rGO}$ composite. The synthesized VS_4 nanoparticles with the size of ~100 nm are distributed on rGO sheets. The EDS mapping displays the homogeneous distribution of V and S elements on the rGO. The HRTEM image (Figure 1f) shows the spacing of 5.58 and 5.95 Å (corresponding well with (110) and (002) crystal plane of monoclinic VS_4 , respectively) and

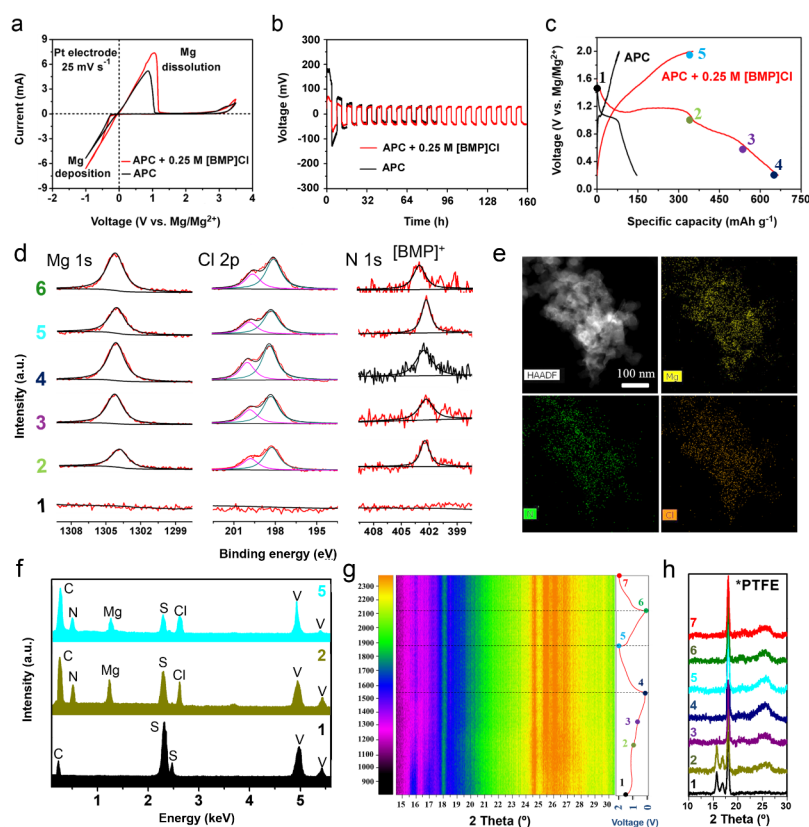


Figure 2. (a) CVs (25 mV s^{-1}) recorded on a Pt electrode in APC with and without [BMP]Cl, (b) voltage–time curves at the current of $20 \mu\text{A}$, (c) first cycle discharge/charge voltage profiles of the Mg– VS_4 @rGO cells at the current density of 50 mA g^{-1} between 0.2 and 2 V (stages 1–5 are pristine VS_4 @rGO, discharged to 1.0, 0.6, 0.2 V and charged to 2 V, respectively), (d) XPS spectra of Mg 1s, Cl 2p, and N 1s, for stages 1–6 (stage 6 is discharged to 0.2 V in the second cycle), (e) the EDS color mapping images about Mg, N, and Cl elements of VS_4 @rGO discharged to 0.2 V in APC with [BMP]Cl, (f) EDS spectra for stages of 1, 2, and 5, (g) in situ XRD characterization and corresponding galvanostatic voltage profile for the first two cycles, and (h) ex situ XRD.

graphene sheets, which confirms the good combination of VS_4 nanoparticles with amorphous graphene.

The electrochemical performance of the APC electrolyte with and without [BMP]Cl was investigated by cyclic voltammograms (CVs, Figure 2a) at a scan rate of 25 mV s^{-1} in the three-electrode beaker cell. As shown in Figure 2a, the APC electrolyte with [BMP]Cl exhibited higher enclosed area and peak current than those of pure APC, which represent higher capacity and activity. Both the electrolytes display reversible Mg deposition–dissolution processes with high efficiencies (100 and 95.6%, respectively) and high anodic stability (above 2.5 V), which guarantee the practical use in the full cell. Figure 2b displays the typical voltage–time curves of both electrolytes in the two Mg electrode cells at the current of $20 \mu\text{A}$. The batteries were first charged with the time of 4 h, and the APC electrolyte with [BMP]Cl shows a smaller initial overpotential for Mg deposition than the pure APC electrolyte (73 and 183 mV, respectively). Within three cycles, both electrolytes reach a stable state with a low overpotential of about 34 mV. These results demonstrate that the APC electrolyte with the addition of [BMP]Cl can preserve the electrochemical properties of APC and shows better performance than the pure APC electrolyte. Figure 2c shows the comparison of the initial discharge/charge curves between two electrolytes in Mg– VS_4 @rGO cells at 50 mA g^{-1} . With the addition of [BMP]Cl, the discharge profile displays a much longer plateau ($\sim 320 \text{ mA h g}^{-1}$) at about 1.15 V and a slope ($\sim 200 \text{ mA h g}^{-1}$) at about 0.8 V, resulting in much higher

capacity of $665.4 \text{ mA h g}^{-1}$. However, the low capacity of $\sim 150 \text{ mA h g}^{-1}$ is obtained in the APC system. It can be noticed that an irreversible reaction exists in the discharge process and results in much lower charge capacity ($353.3 \text{ mA h g}^{-1}$) in the charge process. The similar behavior of VS_4 @rGO as well as some other transition-metal sulphides can also be found in other battery systems.^{34–36} In order to further confirm the irreversibility of the reaction at about 1.15 V, we narrowed the electrochemical window from 0.2–2 to 0.8–2 V to exclude the side effect below 0.8 V. As shown in Figure S1, VS_4 @rGO exhibits a high initial discharge capacity of $412.8 \text{ mA h g}^{-1}$ and a large decay in the following cycles (lower than 110 mA h g^{-1} , Figure S1a). Figure S1b also shows the disappearance of the plateau at about 1.15 V after the initial discharge process.

With the addition of [BMP]Cl, VS_4 @rGO displays much higher discharge capacity which may be caused by the intercalation of $[\text{BMP}]^+$ and its effect on the VS_4 @rGO structure. To investigate the reason for the higher capacities, XPS and EDS were conducted to confirm the intercalation species at various stages. All the electrodes were washed thoroughly with THF in the glovebox to remove the electrolytes. The XPS spectra (Figure 2d) show the signals of Cl, Mg, and N at stage 2. The existence of the N element is attributed to the intercalation of $[\text{BMP}]^+$, and the atomic ratio of Mg to Cl is close to 1:1, indicating the intercalation of MgCl^+ . In addition, the EDS results (Figure 2e,f) agree well with the ones of XPS and ICP tests (Table S2). Figure 2d shows that the peak intensities of Cl and Mg further increase

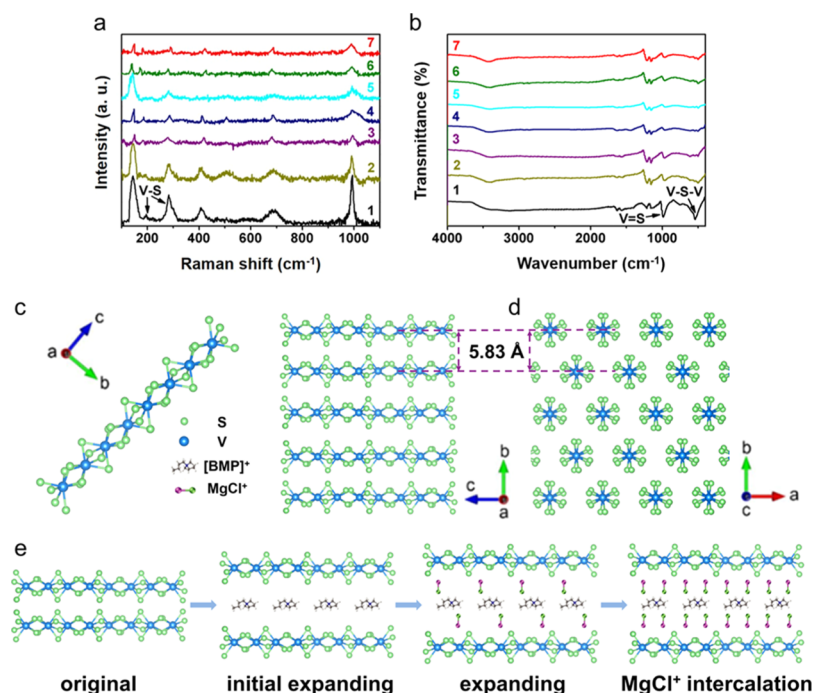


Figure 3. (a) Raman and (b) FTIR spectrum of VS_4 @rGO for stages 1–7, (c,d) detailed structure of the chain-like VS_4 (side-view and top view), and (e) schematic of the structural evolution of neighboring chains in the discharge process (including expanding and intercalation process).

when discharged to stage 4 and decrease again when charged to stage 5, while the N 1s peak has little change. The results indicate that only MgCl^+ intercalation/deintercalation occurs from stage 2 to 5. The remaining $[\text{BMP}]^+$ and partial MgCl^+ in VS_4 @rGO at stage 5 are responsible for the irreversible capacity loss at the initial discharge process. However, in the EDS elemental mappings of VS_4 @rGO discharged to 0.2 V in the APC electrolyte without $[\text{BMP}]\text{Cl}$ addition (Figure S2), only the Mg element is detected, and the Cl and N elements are absent, demonstrating that the inserted species is Mg^{2+} . In comparison, the pristine VS_4 @rGO was immersed in the APC electrolyte with $[\text{BMP}]\text{Cl}$ for 24 h, and the same washing/drying process was conducted to test the existence of $[\text{BMP}]\text{Cl}$ through EDS mapping (Figure S3). The absence of Mg, N, and Cl elements confirms the removal of electrolyte by the washing/drying process. These results confirm that the intercalation of $[\text{BMP}]^+$ into VS_4 changed the intercalation species (from Mg^{2+} to MgCl^+) during the magnesium storage.

To further investigate the structural evolution of VS_4 @rGO during the processes of $[\text{BMP}]^+$ and MgCl^+ insertion/extraction, time-resolved in situ XRD was conducted. Figure 2g displays the results and the corresponding discharge/charge curves of the first two cycles. There is little change in the XRD patterns before being discharged to 1.0 V (about 320 mA h g^{-1}) in the discharge process, which represents no obvious structural change with the evolution of $[\text{BMP}]_x(\text{MgCl})_y\text{VS}_4$ @rGO. The high structural stability with large discharge capacity is attributed to the large interchain distances and weak connection of van der Waals bonding between chains, which can promote the charge transfer kinetics and accommodate the inserted ions.³⁷ The inserted ions push the neighboring chains apart, just like what happens with interlayers in layered materials.²⁹ With the discharge going on, the two main peaks of VS_4 located at 15.8° and 17.0° corresponding to the (110) and (020) lattice plane, respectively, become weaker and disappeared in the end. With the further intercalation of MgCl^+

ions, the interchain spaces were expanded and further been pushed apart to a certain degree. In the charging process, there was little change in the XRD patterns, and the main peaks of VS_4 did not appear, demonstrating the irreversible reaction in the first discharge process. The corresponding ex situ XRD (Figure 2h) analysis exhibited the same results.

In order to investigate the structural evolution of VS_4 @rGO, ex situ Raman and FTIR spectroscopies were conducted. Figure 3a shows the Raman spectra of original and different states of VS_4 @rGO. It should be noted that the Raman spectrum of original VS_4 @rGO contains all the intensive vibration modes of VS_4 , same as those published in previous papers.^{29,38} The identified bonds located at 192 and 279 cm^{-1} are ascribed to V–S stretching (A1) and bending (B1) modes.³⁸ The intensities of the two peaks were decreased with the ions intercalated, suggesting weakening of V–S stretching and bending. When charged to 2.0 V, the two peaks recovered to their original status to some extent, indicating the reversibility of the V–S stretching. In the subsequent cycle, the Raman spectra exhibited the same trends. FTIR spectra of the VS_4 @rGO at the corresponding states were also measured (Figure 3b). The bonds located at about 545 and 997 cm^{-1} are the resemblance of the V–S–V bending mode and the terminal V=S stretches, respectively.³⁸ At the original stage, both the two peaks are sharp and easy to be distinguished and they become weaker in the discharge process. In the subsequent cycles, all the peaks demonstrate little change. The slight shift of the V–S–V bending mode may be caused by the little oxidation of samples.³⁸ The Raman and FTIR results indicate that the bonds between specific atoms have little change during the expansion and the following discharge/charge processes, which means the retention of chains in the structure.

A schematic illustration about the structural evolution of VS_4 at different stages is shown in Figure 3e. The obtained VS_4 is a linear chain structure; Figure 3c,d exhibits the detailed chains

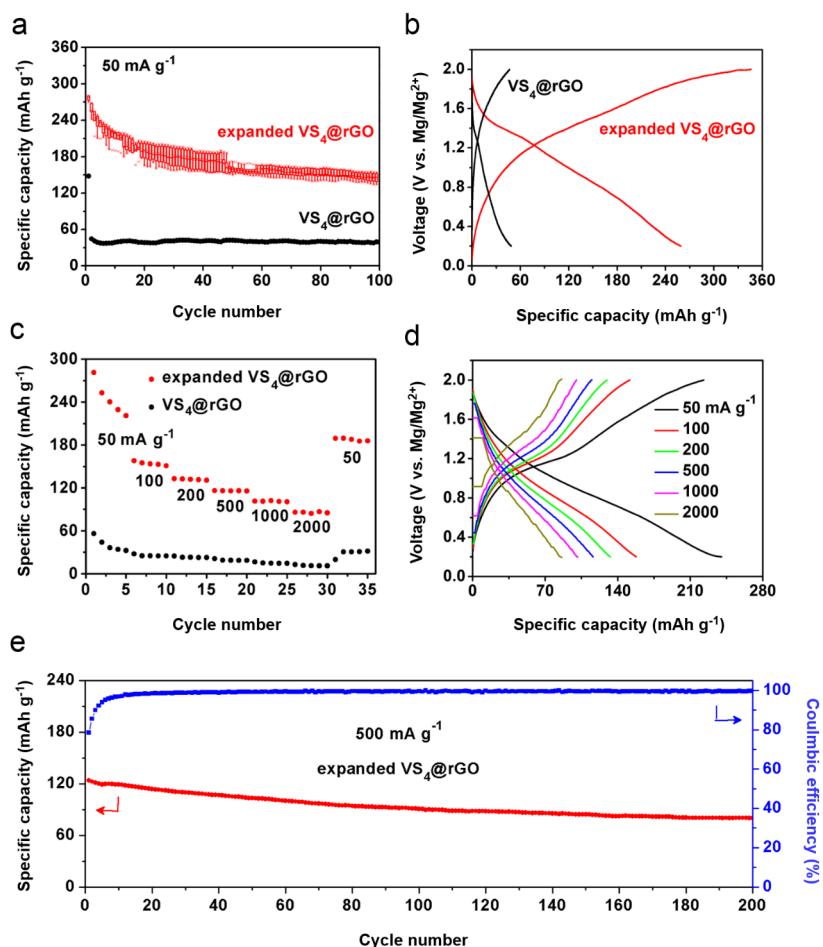


Figure 4. (a) Cycling performance of pristine $\text{VS}_4@\text{rGO}$ and expanded $\text{VS}_4@\text{rGO}$ (box plots) of electrodes at 50 mA g^{-1} , (b) corresponding charge/discharge curves of the first cycle, (c) rate capability from 50 to 2000 mA g^{-1} , (d) corresponding voltage profiles of expanded $\text{VS}_4@\text{rGO}$, and (e) cycling performance at 500 mA g^{-1} of expanded $\text{VS}_4@\text{rGO}$.

in different views. The neighboring chains are connected with weak van der Waals forces, which have a large distance of 5.83 \AA . In this respect, a loosely stacked structure is formed, and a large number of potential sites are provided between chains.³⁸ To give further evidence of the interchain expansion with the intercalation of $[\text{BMP}]^+$, first-principles computations based on density functional theory were conducted using the CASTEP code in Materials Studio (version 2017 R2) of Accelrys Inc (more details are provided in the Supporting Information). When the $[\text{BMP}]^+$ intercalated into the VS_4 interchains, the distance is expanded to 12.52 \AA with the volume expansion of 130.19%. In this way, MgCl^+ ions begin to insert into the structure, and the distance is further expanded. In the following discharge, a large number of MgCl^+ intercalation caused the phase change. It is worth mentioning that the chains are not destroyed for the unchanged peak locations of Raman and FTIR. After these steps, a small amount of $[\text{BMP}]^+$ ions stayed between the chains of VS_4 (denoted as expanded $\text{VS}_4@\text{rGO}$), which contribute greatly to the reversible insertion/extraction of MgCl^+ .

The electrochemical performances of expanded $\text{VS}_4@\text{rGO}$ and unexpanded $\text{VS}_4@\text{rGO}$ were attained to identify the improvement. As shown in Figure S4, expanded $\text{VS}_4@\text{rGO}$ demonstrates a high reversible capacity of $268.3 \text{ mA h g}^{-1}$ (higher than that of branched VS_4 nanodendrites, 195 mA h

g^{-1} , ref 39) and maintains $147.2 \text{ mA h g}^{-1}$ after 100 cycles at 50 mA g^{-1} based on the mass of $\text{VS}_4@\text{rGO}$. It is 225.2 and $124.1 \text{ mA h g}^{-1}$ when calculated based on the mass of $[\text{BMP}]0.26\text{VS}_4@\text{rGO}$ (calculated from Table S2 and Figure S5). To confirm the repetitions of the electrochemical performance based on expanded $\text{VS}_4@\text{rGO}$, the box plots about the electrochemical performance are provided in Figure 4a. However, pristine $\text{VS}_4@\text{rGO}$ only exhibited about 40 mA h g^{-1} after the first cycle (Figure 4a). Figure 4b displays the discharge/charge curves of $\text{VS}_4@\text{rGO}$. The expanded $\text{VS}_4@\text{rGO}$ exhibits remarkable rate capability (Figure 4c). When the current densities increased to 100, 200, 500, and 1000 mA g^{-1} , the discharge capacities are as high as 157.9, 132.8, 116.2, and $101.4 \text{ mA h g}^{-1}$, respectively. Even at a high current density of 2000 mA g^{-1} , a reversible discharge capacity of 85.9 mA h g^{-1} (or 70.9 mA h g^{-1} based on the mass of $[\text{BMP}]0.26\text{VS}_4@\text{rGO}$) is still achieved. When the current density is recovered to 50 mA g^{-1} , the capacity recovers to $187.8 \text{ mA h g}^{-1}$. In comparison, pristine $\text{VS}_4@\text{rGO}$ shows much lower capacity at all current densities. The corresponding discharge/charge profiles of expanded $\text{VS}_4@\text{rGO}$ at various current densities are shown in Figure 4d. The long-cycle performance of expanded $\text{VS}_4@\text{rGO}$ at 500 mA g^{-1} is exhibited in Figure 4e. The initial discharge capacity is as high as $123.8 \text{ mA h g}^{-1}$ and still remains 78.9 mA h g^{-1} even after 200 cycles, the capacity

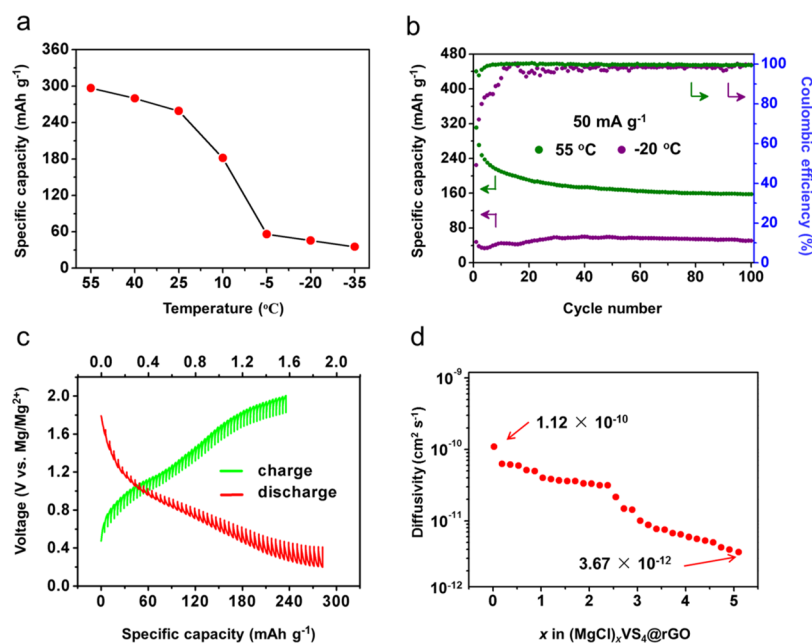


Figure 5. (a) Capacity–temperature curve between -35 and 55 °C of expanded VS_4 @rGO, (b) cycling performance with the current density of 50 mA g^{-1} at 55 and -20 °C, (c) GITT curve of expanded VS_4 @rGO in APC with the 0.25 M [BMP]Cl electrolyte at room temperature, and (d) MgCl^+ diffusivity vs the state of discharge.

retention is 63.7% compared with the first cycle. It is worth mentioning that the coulombic efficiency remains higher than 98% except for the first few cycles. The corresponding discharge/charge profiles are shown in Figure S6. To identify the improved Mg-storage performance of expanded VS_4 @rGO and exclude the side effect of $[\text{BMP}]^+$ ions in the electrolyte during cycling, the VS_4 @rGO at stage 5 is used to fabricate a new cell in the pure APC electrolyte. As shown in Figure S7, the charge/discharge curves of the first cycle indicating the capacity can be retained and is much higher than the unexpanded VS_4 @rGO.

The potential application of expanded VS_4 @rGO as the cathode material of the Mg full cell at high and low temperatures was also studied (Figure 5a). A high capacity of 296.6 mA h g^{-1} is obtained when the temperature increases to 55 °C, corresponding to the insertion of about 1.97 MgCl^+ per unit of VS_4 @rGO. Surprisingly, the cell demonstrated 35.4 mA h g^{-1} even at relatively low temperature of -35 °C. More importantly, the expanded VS_4 @rGO showed excellent temperature adaptability (Figure 5b). At 55 °C, a higher discharge capacity of 156.5 mA h g^{-1} is retained after 100 cycles. Even at -20 °C, the capacity of about 40 mA h g^{-1} is remained in 100 cycles. The coulombic efficiency is low at first and improved to about 95% after 30 cycles, which may be caused by the sluggish kinetics of the electrolyte at low temperatures. To investigate the origin of the excellent rate capability and high discharge capacity, the kinetics of MgCl^+ solid-state diffusion in expanded VS_4 @rGO were studied via GITT after the battery is stabilized.^{25,40} In the GITT measurement (Figure 5c), the VS_4 @rGO displays a high discharge capacity of 282.4 mA h g^{-1} , corresponding to 1.87 MgCl^+ insertion per formula. The MgCl^+ diffusivity (Figure 5d) decreases from 1.12×10^{-10} to 3.67×10^{-12} $\text{cm}^2 \text{s}^{-1}$ with the increasing of MgCl^+ concentration. The average MgCl^+ diffusivity during the intercalation process is about 2.72×10^{-11} $\text{cm}^2 \text{s}^{-1}$, which is as fast as TiS_2 (MgCl^+ diffusivity, 10^{-11} $\text{cm}^2 \text{s}^{-1}$) and one order of magnitude higher than that of

Mo_6S_8 (Mg^{2+} diffusivity, 10^{-12} $\text{cm}^2 \text{s}^{-1}$) and poly(ethylene oxide)-intercalated MoS_2 (Mg^{2+} diffusivity, 4.4×10^{-12} $\text{cm}^2 \text{s}^{-1}$).^{27,41,42} The calculated Mg^{2+} diffusivity in pristine VS_4 @rGO is at the level of 3.21×10^{-13} $\text{cm}^2 \text{s}^{-1}$ (Figure S8), which is much lower than that of MgCl^+ in expanded VS_4 @rGO. The expanded interchain distances enabled fast kinetics of MgCl^+ ions, resulting in the higher specific capacity and excellent rate performance.

CONCLUSIONS

In conclusion, we conducted the optimization of chainlike structure VS_4 through in situ preintercalation of $[\text{BMP}]^+$ to expand the interchain distances and systematically investigated the expanding process. The expanded VS_4 @rGO sample exhibits higher Mg storage capacity (268.3 mA h g^{-1}), remarkable rate performance (85.9 mA h g^{-1} at 2000 mA g^{-1}), and outstanding temperature adaptability (-35 to 55 °C) among the reported cathodes of MBs. Our work demonstrates that the intercalation species have a direct relation with the interchain distance and a large impact on the electrochemical performance. Compared with the reported Mg^{2+} intercalation cathodes, the fast kinetics of MgCl^+ enables the larger specific capacity and better rate capability. The successful utilization of MgCl^+ ion intercalation into host materials indicates a promising direction to improve the performance of MBs.

ASSOCIATED CONTENT

Supporting Information

The Supporting Information is available free of charge on the ACS Publications website at DOI: 10.1021/acsami.9b09592.

Cycling performance and voltage profiles of VS_4 @rGO between the voltage of 0.8 – 2 V, EDS color mapping images of VS_4 @rGO discharged to 0.2 V in the APC electrolyte, EDS color mapping images of VS_4 @rGO immersed in the APC electrolyte with [BMP]Cl for 24 h and conducted the same washing/drying process, cycling

performance of expanded VS₄@rGO at 50 mA g⁻¹, TGA for the samples of state 1 and 4 in a nitrogen flow, voltage profiles of expanded VS₄@rGO in 0.25 M APC with 0.25 M [BMP]Cl, charge/discharge curves of the new fabricated cell using pristine VS₄@rGO and the expanded VS₄@rGO at stage 5 in the pure APC electrolyte, Mg ion diffusivity versus the state of discharge in the pure APC electrolyte, detail of first-principles calculations, and characterization of [BMP]_x(MgCl)_yVS₄@rGO based on EDS and ICP-optical emission spectroscopy analysis (PDF)

AUTHOR INFORMATION

Corresponding Authors

*E-mail: anqinyou86@whut.edu.cn (Q.A.).

*E-mail: mlq518@whut.edu.cn (L.M.).

ORCID

Liqiang Mai: 0000-0003-4259-7725

Author Contributions

The manuscript was written through contributions of all the authors. All the authors have given approval to the final version of the manuscript.

Notes

The authors declare no competing financial interest.

ACKNOWLEDGMENTS

This work was supported by the National Key Research and Development Program of China (2016YFA0202603, 2016YFA0202601), the National Natural Science Fund for Distinguished Young Scholars (51425204), the Project funded by China Postdoctoral Science Foundation (20181j204), the National Natural Science Foundation of China (51521001, 51602239), the Programme of Introducing Talents of Discipline to Universities (B17034), the International Science & Technology Cooperation Program of China (2013DFA50840), the Yellow Crane Talent (Science & Technology) Program of Wuhan City, and the Fundamental Research Funds for the Central Universities (WUT: 2017III009, 2017III005).

REFERENCES

- (1) Kim, J.; Seo, D.-H.; Kim, H.; Park, I.; Yoo, J.-K.; Jung, S.-K.; Park, Y.-U.; Goddard III, W. A.; Kang, K. Unexpected discovery of low-cost maricite NaFePO₄ as a high-performance electrode for Na-ion batteries. *Energy Environ. Sci.* **2015**, *8*, 540–545.
- (2) Albertus, P.; Babinec, S.; Litzelman, S.; Newman, A. Status and Challenges in Enabling the Lithium Metal Electrode for High-energy and Low-cost Rechargeable Batteries. *Nat. Energy* **2017**, *3*, 16–21.
- (3) Wang, Y.; Liu, J.; Lee, B.; Qiao, R.; Yang, Z.; Xu, S.; Yu, X.; Gu, L.; Hu, Y. S.; Yang, W.; Kang, K.; Li, H.; Yang, X. Q.; Chen, L.; Huang, X. Ti-substituted Tunnel-type Na_{0.44}MnO₂ Oxide as a Negative Electrode for Aqueous Sodium-ion Batteries. *Nat. Commun.* **2015**, *6*, 6401–6410.
- (4) Yin, Y.; Xiong, F.; Pei, C.; Xu, Y.; An, Q.; Tan, S.; Zhuang, Z.; Sheng, J.; Li, Q.; Mai, L. Robust Three-dimensional Graphene Skeleton Encapsulated Na₃V₂O₇(PO₄)₂F Nanoparticles as a High-rate and Long-life Cathode of Sodium-ion Batteries. *Nano Energy* **2017**, *41*, 452–459.
- (5) Liu, J.; Yu, L.; Wu, C.; Wen, Y.; Yin, K.; Chiang, F.-K.; Hu, R.; Liu, J.; Sun, L.; Gu, L.; Maier, J.; Yu, Y.; Zhu, M. New Nanoconfined Galvanic Replacement Synthesis of Hollow Sb@C Yolk-Shell Spheres Constituting a Stable Anode for High-Rate Li/Na-Ion Batteries. *Nano Lett.* **2017**, *17*, 2034–2042.

- (6) Pan, H.; Chen, J.; Cao, R.; Murugesan, V.; Rajput, N. N.; Han, K. S.; Persson, K.; Estevez, L.; Engelhard, M. H.; Zhang, J.-G.; Mueller, K. T.; Cui, Y.; Shao, Y. Non-encapsulation approach for high-performance Li-S batteries through controlled nucleation and growth. *Nat. Energy* **2017**, *2*, 813–820.

- (7) Liu, T. J.; Mohtadi, R.; Arthur, T. S.; Mizuno, F.; Zhang, R.; Shirai, S.; Kampf, J. W. Boron Clusters as Highly Stable Magnesium-Battery Electrolytes. *Angew. Chem., Int. Ed.* **2014**, *126*, 3237–3241.

- (8) Zhao-Karger, Z.; Zhao, X.; Wang, D.; Diemant, T.; Behm, R. J.; Fichtner, M. Performance Improvement of Magnesium Sulfur Batteries with Modified Non-Nucleophilic Electrolytes. *Adv. Energy Mater.* **2015**, *5*, 1401155.

- (9) Dong, H.; Liang, Y.; Tutusaus, O.; Mohtadi, R.; Zhang, Y.; Hao, F.; Yao, Y. Directing Mg-Storage Chemistry in Organic Polymers toward High-Energy Mg Batteries. *Joule* **2019**, *3*, 782–793.

- (10) Yoo, H. D.; Shterenberg, I.; Gofer, Y.; Gershinshy, G.; Pour, N.; Aurbach, D. Mg Rechargeable Batteries: an on-going Challenge. *Energy Environ. Sci.* **2013**, *6*, 2265–2279.

- (11) Cheng, Y.; Shao, Y.; Parent, L. R.; Sushko, M. L.; Li, G.; Sushko, P. V.; Browning, N. D.; Wang, C.; Liu, J. Interface Promoted Reversible Mg Insertion in Nanostructured Tin-Antimony Alloys. *Adv. Mater.* **2015**, *27*, 6598–6605.

- (12) Guo, Y.-s.; Zhang, F.; Yang, J.; Wang, F.-f.; Nuli, Y.; Hirano, S.-i. Boron-based Electrolyte Solutions with Wide Electrochemical Windows for Rechargeable Magnesium Batteries. *Energy Environ. Sci.* **2012**, *5*, 9100–9106.

- (13) Wu, N.; Yang, Z.-Z.; Yao, H.-R.; Yin, Y.-X.; Gu, L.; Guo, Y.-G. Improving the Electrochemical Performance of the Li₄Ti₅O₁₂ Electrode in a Rechargeable Magnesium Battery by Lithium-Magnesium Co-Intercalation. *Angew. Chem., Int. Ed.* **2015**, *54*, 5757–5761.

- (14) Wang, W.; Liu, L.; Wang, P.-F.; Zuo, T.-T.; Yin, Y.-X.; Wu, N.; Zhou, J.-M.; Wei, Y.; Guo, Y.-G. A Novel Bismuth-based Anode Material with a Stable Alloying Process by the Space Confinement of an *In Situ* Conversion Reaction for a Rechargeable Magnesium Ion Battery. *Chem. Commun.* **2018**, *54*, 1714–1717.

- (15) Shao, Y.; Gu, M.; Li, X.; Nie, Z.; Zuo, P.; Li, G.; Liu, T.; Xiao, J.; Cheng, Y.; Wang, C.; Zhang, J.-G.; Liu, J. Highly Reversible Mg Insertion in Nanostructured Bi for Mg Ion batteries. *Nano Lett.* **2014**, *14*, 255–260.

- (16) Muldoon, J.; Bucur, C. B.; Gregory, T. Quest for Nonaqueous Multivalent Secondary Batteries: Magnesium and Beyond. *Chem. Rev.* **2014**, *114*, 11683–11720.

- (17) Cheng, Y.; Shao, Y.; Raju, V.; Ji, X.; Mehdi, B. L.; Han, K. S.; Engelhard, M. H.; Li, G.; Browning, N. D.; Mueller, K. T.; Liu, J. Molecular Storage of Mg Ions with Vanadium Oxide Nanoclusters. *Adv. Funct. Mater.* **2016**, *26*, 3446–3453.

- (18) Levi, E.; Gofer, Y.; Aurbach, D. On the Way to Rechargeable Mg Batteries: The Challenge of New Cathode Materials. *Chem. Mater.* **2010**, *22*, 860–868.

- (19) Miao, X.; Chen, Z.; Wang, N.; Nuli, Y.; Wang, J.; Yang, J.; Hirano, S.-i. Electrospun V₂MoO₈ as a Cathode Material for Rechargeable Batteries with Mg Metal Anode. *Nano Energy* **2017**, *34*, 26–35.

- (20) Aurbach, D.; Lu, Z.; Schechter, A.; Gofer, Y.; Gizbar, H.; Turgeman, R.; Cohen, Y.; Moshkovich, M.; Levi, E. Prototype Systems for Rechargeable Magnesium Batteries. *Nature* **2000**, *407*, 724–727.

- (21) Sun, X.; Bonnicksen, P.; Duffort, V.; Liu, M.; Rong, Z.; Persson, K. A.; Ceder, G.; Nazar, L. F. A High Capacity Thiospinel Cathode for Mg Batteries. *Energy Environ. Sci.* **2016**, *9*, 2273–2277.

- (22) Gofer, Y.; Chusid, O.; Aurbach, D. Magnesium Batteries (Secondary and Primary). *Encyclopedia of Electrochemical Power Sources*; Elsevier, 2009; pp 285–301.

- (23) Levi, M.; Lanci, E.; Levi, E.; Gizbar, H.; Gofer, Y.; Aurbach, D. The effect of the anionic framework of MoX Chevrel Phase (X=S, Se) on the thermodynamics and the kinetics of the electrochemical insertion of Mg ions. *Solid State Ionics* **2005**, *176*, 1695–1699.

- (24) Gautam, G. S.; Canepa, P.; Abdellahi, A.; Urban, A.; Malik, R.; Ceder, G. The Intercalation Phase Diagram of Mg in V_2O_5 from First-Principles. *Chem. Mater.* **2015**, *27*, 3733–3742.
- (25) An, Q.; Li, Y.; Deog Yoo, H.; Chen, S.; Ru, Q.; Mai, L.; Yao, Y. Graphene Decorated Vanadium Oxide Nanowire Aerogel for Long-cycle-life Magnesium Battery Cathodes. *Nano Energy* **2015**, *18*, 265–272.
- (26) Nam, K. W.; Kim, S.; Lee, S.; Salama, M.; Shterenberg, I.; Gofer, Y.; Kim, J.-S.; Yang, E.; Park, C. S.; Kim, J.-S.; Lee, S.-S.; Chang, W.-S.; Doo, S.-G.; Jo, Y. N.; Jung, Y.; Aurbach, D.; Choi, J. W. The High Performance of Crystal Water Containing Manganese Birnessite Cathodes for Magnesium Batteries. *Nano Lett.* **2015**, *15*, 4071–4079.
- (27) Yoo, H. D.; Liang, Y.; Dong, H.; Lin, J.; Wang, H.; Liu, Y.; Ma, L.; Wu, T.; Li, Y.; Ru, Q.; Jing, Y.; An, Q.; Zhou, W.; Guo, J.; Lu, J.; Pantelides, S. T.; Qian, X.; Yao, Y. Fast Kinetics of Magnesium Monochloride Cations in Interlayer-expanded Titanium Disulfide for Magnesium Rechargeable Batteries. *Nat. Commun.* **2017**, *8*, 339.
- (28) Zhou, L.; Liu, Q.; Zhang, Z.; Zhang, K.; Xiong, F.; Tan, S.; An, Q.; Kang, Y. M.; Zhou, Z.; Mai, L. Interlayer-Spacing-Regulated $VOPO_4$ Nanosheets with Fast Kinetics for High-Capacity and Durable Rechargeable Magnesium Batteries. *Adv. Mater.* **2018**, *30*, No. e1801984.
- (29) Kozlova, M. N.; Mironov, Y. V.; Grayfer, E. D.; Smolentsev, A. I.; Zaikovskii, V. I.; Nebogatikova, N. A.; Podlipskaya, T. Y.; Fedorov, V. E. Synthesis, Crystal Structure, and Colloidal Dispersions of Vanadium Tetrasulfide (VS_4). *Chem.—Eur. J.* **2015**, *21*, 4639–4645.
- (30) Rout, C. S.; Kim, B.-H.; Xu, X.; Yang, J.; Jeong, H. Y.; Odkhuu, D.; Park, N.; Cho, J.; Shin, H. S. Synthesis and Characterization of Patronite Form of Vanadium Sulfide on Graphitic Layer. *J. Am. Chem. Soc.* **2013**, *135*, 8720–8725.
- (31) Sun, R.; Wei, Q.; Li, Q.; Luo, W.; An, Q.; Sheng, J.; Wang, D.; Chen, W.; Mai, L. Vanadium sulfide on reduced graphene oxide layer as a promising anode for sodium ion battery. *ACS Appl. Mater. Interfaces* **2015**, *7*, 20902–20908.
- (32) Mizrahi, O.; Amir, N.; Pollak, E.; Chusid, O.; Marks, V.; Gottlieb, H.; Larush, L.; Zinigrad, E.; Aurbach, D. Electrolyte solutions with a wide electrochemical window for rechargeable magnesium batteries. *J. Electrochem. Soc.* **2008**, *155*, A103–A109.
- (33) Guo, W.; Wu, D. Facile Synthesis of VS_4 /graphene Nanocomposites and Their Visible-light-driven Photocatalytic Water Splitting Activities. *Int. J. Hydrogen Energy* **2014**, *39*, 16832–16840.
- (34) Zhang, S. S. The redox mechanism of FeS_2 in non-aqueous electrolytes for lithium and sodium batteries. *J. Mater. Chem. A* **2015**, *3*, 7689–7694.
- (35) Qu, B.; Ma, C.; Ji, G.; Xu, C.; Xu, J.; Meng, Y. S.; Wang, T.; Lee, J. Y. Layered SnS_2 -Reduced Graphene Oxide Composite—A High-Capacity, High-Rate, and Long-Cycle Life Sodium-Ion Battery Anode Material. *Adv. Mater.* **2014**, *26*, 3854–3859.
- (36) Zhou, T.; Pang, W. K.; Zhang, C.; Yang, J.; Chen, Z.; Liu, H. K.; Guo, Z. Enhanced Sodium-Ion Battery Performance by Structural Phase Transition from Two-Dimensional Hexagonal- SnS_2 to Orthorhombic- SnS . *ACS Nano* **2014**, *8*, 8323–8333.
- (37) Zhou, Y.; Li, Y.; Yang, J.; Tian, J.; Xu, H.; Yang, J.; Fan, W. Conductive Polymer-Coated VS_4 Submicrospheres As Advanced Electrode Materials in Lithium-Ion Batteries. *ACS Appl. Mater. Interfaces* **2016**, *8*, 18797–18805.
- (38) Lui, G.; Jiang, G.; Duan, A.; Broughton, J.; Zhang, J.; Fowler, M. W.; Yu, A. Synthesis and Characterization of Template-Free VS_4 Nanostructured Materials with Potential Application in Photocatalysis. *Ind. Eng. Chem. Res.* **2015**, *54*, 2682–2689.
- (39) Wang, Y.; Liu, Z.; Wang, C.; Yi, X.; Chen, R.; Ma, L.; Hu, Y.; Zhu, G.; Chen, T.; Tie, Z.; Ma, J.; Liu, J.; Jin, Z. Highly Branched VS_4 Nanodendrites with 1D Atomic-Chain Structure as a Promising Cathode Material for Long-Cycling Magnesium Batteries. *Adv. Mater.* **2018**, *30*, No. e1802563.
- (40) Pei, C.; Xiong, F.; Sheng, J.; Yin, Y.; Tan, S.; Wang, D.; Han, C.; An, Q.; Mai, L. VO_2 Nanoflakes as the Cathode Material of Hybrid Magnesium-Lithium-Ion Batteries with High Energy Density. *ACS Appl. Mater. Interfaces* **2017**, *9*, 17060–17066.
- (41) Levi, M. D.; Lancry, E.; Gizbar, H.; Gofer, Y.; Levi, E.; Aurbach, D. Phase transitions and diffusion kinetics during Mg^{2+} - and Li^+ -ion insertions into the Mo_6S_8 chevrel phase compound studied by PITT. *Electrochim. Acta* **2004**, *49*, 3201–3209.
- (42) Liang, Y.; Yoo, H. D.; Li, Y.; Shuai, J.; Calderon, H. A.; Robles Hernandez, F. C.; Grabow, L. C.; Yao, Y. Interlayer-expanded Molybdenum Disulfide Nanocomposites for Electrochemical Magnesium Storage. *Nano Lett.* **2015**, *15*, 2194–2202.